

Localization of Deep Water Formation: Role of Atmospheric Moisture Transport and Geometrical Constraints on Ocean Circulation

DAVID FERREIRA, JOHN MARSHALL, AND JEAN-MICHEL CAMPIN

Department of Earth, Atmospheric and Planetary Science, Massachusetts Institute of Technology, Cambridge, Massachusetts

(Manuscript received 9 April 2009, in final form 4 September 2009)

ABSTRACT

A series of coupled atmosphere–ocean–ice aquaplanet experiments is described in which topological constraints on ocean circulation are introduced to study the role of ocean circulation on the mean climate of the coupled system. It is imagined that the earth is completely covered by an ocean of uniform depth except for the presence or absence of narrow barriers that extend from the bottom of the ocean to the sea surface. The following four configurations are described: Aqua (no land), Ridge (one barrier extends from pole to pole), Drake (one barrier extends from the North Pole to 35°S), and DDrake (two such barriers are set 90° apart and join at the North Pole, separating the ocean into a large basin and a small basin, connected to the south). On moving from Aqua to Ridge to Drake to DDrake, the energy transports in the equilibrium solutions become increasingly “realistic,” culminating in DDrake, which has an uncanny resemblance to the present climate. Remarkably, the zonal-average climates of Drake and DDrake are strikingly similar, exhibiting almost identical heat and freshwater transports, and meridional overturning circulations. However, Drake and DDrake differ dramatically in their regional climates. The small and large basins of DDrake exhibit distinctive Atlantic-like and Pacific-like characteristics, respectively: the small basin is warmer, saltier, and denser at the surface than the large basin, and is the main site of deep water formation with a deep overturning circulation and strong northward ocean heat transport. A sensitivity experiment with DDrake demonstrates that the salinity contrast between the two basins, and hence the localization of deep convection, results from a deficit of precipitation, rather than an excess of evaporation, over the small basin. It is argued that the width of the small basin relative to the zonal fetch of atmospheric precipitation is the key to understanding this salinity contrast.

Finally, it is argued that many gross features of the present climate are consequences of two topological asymmetries that have profound effects on ocean circulation: a meridional asymmetry (circumpolar flow in the Southern Hemisphere; blocked flow in the Northern Hemisphere) and a zonal asymmetry (a small basin and a large basin).

1. Introduction

Many prominent features of the earth’s climate, such as the pattern of westerly winds and trade winds, the Hadley circulation, and the latitude of deserts and temperate zones, are rather insensitive to the detailed distribution (or even presence) of landmasses. The distribution of land, however, affects regional climate by modulating the orographic and diabatic heating of the atmosphere, setting up planetary waves, and organizing its storm tracks. Moreover, the presence of meridional barriers has a profound effect on ocean circulation, supporting zonal pressure gradients and ocean gyres with their associated

western boundary currents and heat transport. Conversely, the absence of meridional boundaries permits massive zonal currents, such as the Antarctic Circumpolar Current, which act as barriers to poleward heat transport. To the extent that ocean circulation plays a role in transporting heat around the globe, and particularly in the meridional direction, one might expect topological constraints on the ocean to play an important role in setting the climate of the planet. Indeed, the role of tectonics in driving climate change in this way is a theme of the paleoclimate literature (see, e.g., Barron et al. 1993).

Here, rather than inquire into the climate of a particular time in the earth’s history, we consider some fundamental aspects of the role of ocean circulation in setting the mean climate of the earth. We investigate the influences of geometrical constraints on ocean circulation

Corresponding author address: David Ferreira, EAPS, MIT, Room 54-1515, 77 Massachusetts Ave., Cambridge, MA 02139.
E-mail: dfer@mit.edu

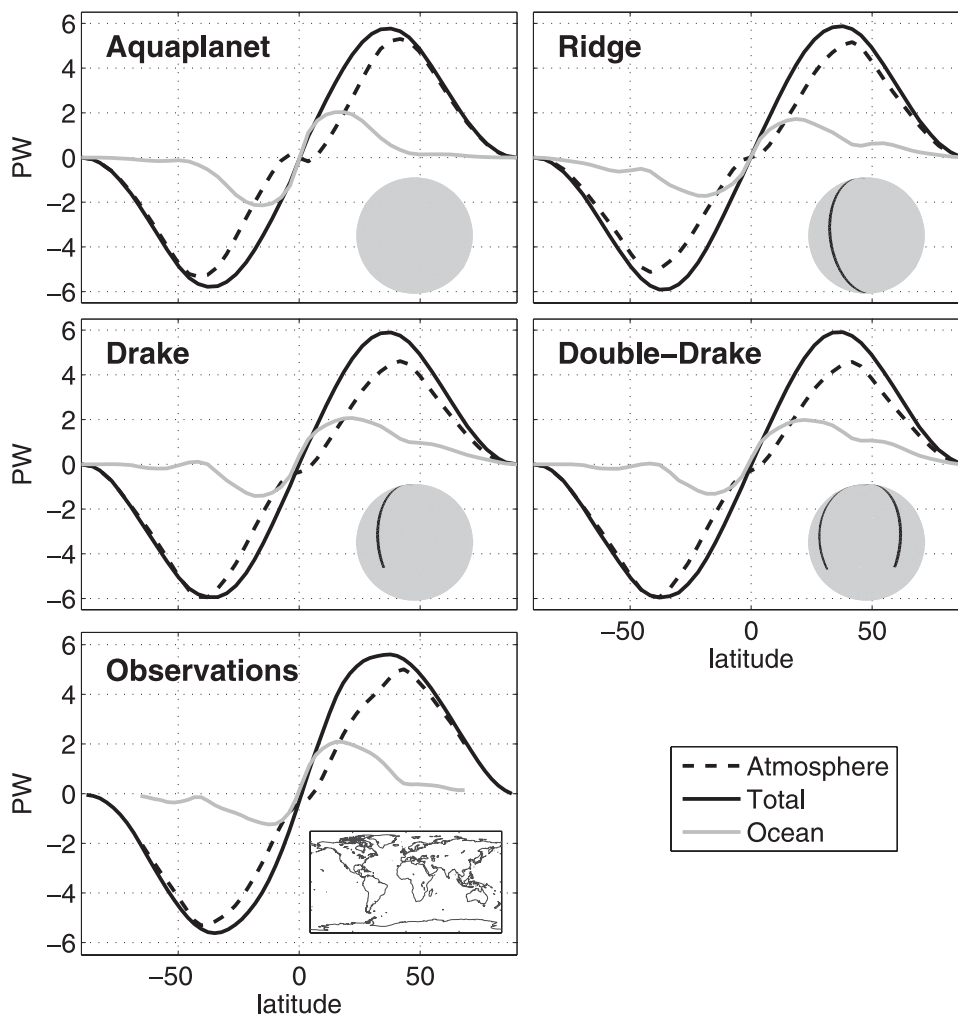


FIG. 1. Atmospheric, oceanic, and total heat transports (PW) for Aqua, Ridge, Drake, and DDrake. The configurations are shown in inserts (see text for details). Estimates of observed transports for the present climate (bottom left) are taken from Trenberth and Caron (2001).

by carrying out a series of experiments with a coupled ocean–atmosphere–sea ice general circulation model (GCM) in which the complexity of landmass distributions is increased in stages. Our goal is to determine a minimal description of the geometrical constraints that captures the essence of the role of the ocean circulation in climate. In this spirit, landmasses are represented schematically as narrow vertical barriers extending from the (assumed flat) seafloor up to the sea surface. These barriers do not extend up into the atmosphere and so have no orographic effect on the atmosphere. Four configurations of increasing complexity are considered: Aqua (an aquaplanet: no land at all), Ridge (one land barrier extending from pole to pole), Drake (one barrier from the North Pole to 35°S), and DDrake (two barriers extending from the North Pole to 35°S, and set 90°

apart). Details of the model configuration are given in section 2 below.

Figure 1 shows the oceanic, atmospheric, and total heat transports of these four configurations, along with their observed counterparts (Trenberth and Caron 2001).¹ First, it is striking that the gross characteristics of the transports, both in magnitude and pattern, are so similar to one another despite these widely differing configurations and, moreover, so similar to that of the observed

¹ This is just one estimate with its associated uncertainties, probably of the order of a few tenths of a PW (see Wunsch 2005). Bryden and Imawaki (2001) discuss in detail the various estimation methods and their biases. Note, however, that we are most concerned here with the meridional structures of heat transports, which exhibit more robustness than absolute magnitudes.

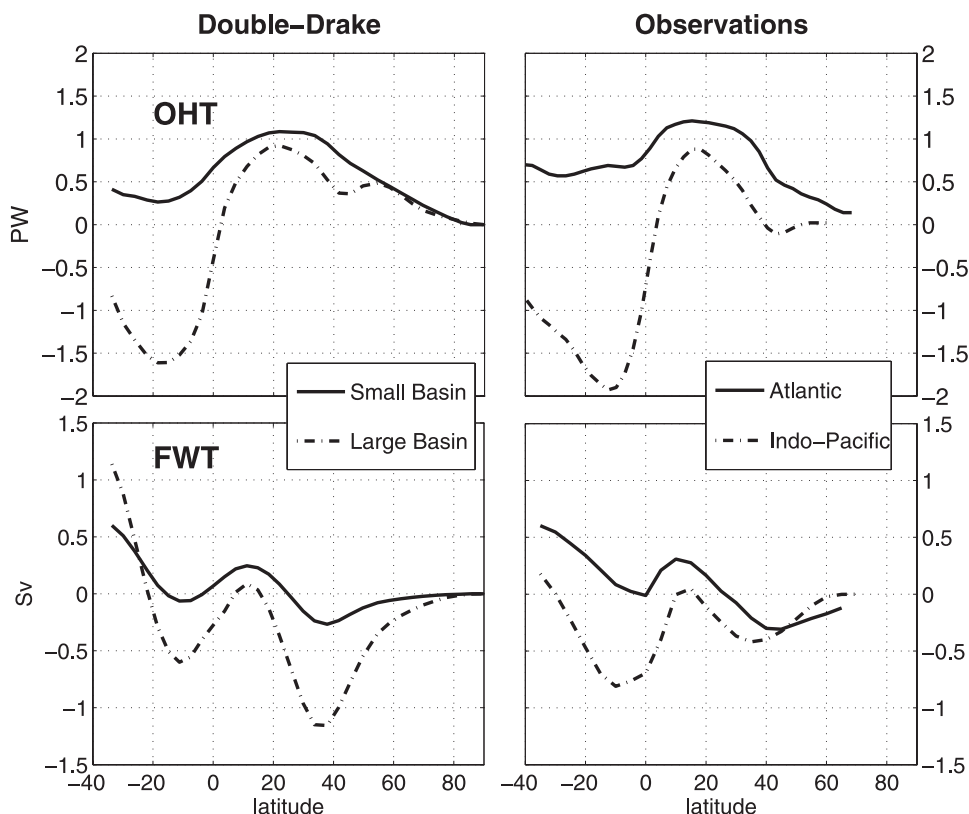


FIG. 2. (top) Ocean heat and (bottom) freshwater transports for (left) the small and large basins of DDrake and (right) the Atlantic and Indo-Pacific sectors. Observations of heat and freshwater transports are taken from Trenberth and Caron (2001) and Wijffels et al. (1992), respectively.

climate. Indeed, as discussed in Enderton and Marshall (2009), the total (ocean + atmosphere) heat transport is almost identical in these calculations. However, upon closer inspection, subtle but rather significant differences in the partition of the heat transport between ocean and atmosphere are evident. These are associated with marked differences in climate. Czaja and Marshall (2006) and Marshall et al. (2007) discuss the heat transport and climate of Aqua, with very weak ocean heat transport (OHT) poleward of 50° . Indeed, one might expect the poles of Aqua to be very much colder than those of Ridge, where ocean gyres can readily transport energy to high latitudes. In fact, as will be described in a forthcoming paper, Aqua exhibits multiple equilibria: a cold solution with large sea ice caps at the poles [the solution discussed in Marshall et al. (2007)] and a warm ice-free solution. Both warm and cold Aqua solutions have vanishingly small OHTs at high latitudes. Here, we present the warm solution that naturally emerges in this series of experiments.

The Drake solution introduces hemispheric asymmetries with a zonally unbounded ocean in the Southern

Hemisphere and a blocked one in the Northern Hemisphere. The Southern Hemisphere OHT is reminiscent of that of Aqua, while the Northern Hemisphere OHT is more similar to that found in Ridge. Additionally, the hemispheric asymmetry allows the development of an interhemispheric overturning circulation in the ocean with sinking over the North Pole and upwelling in the Southern Ocean. The OHT is thus directed more “northward” everywhere and a small cross-equatorial heat transport is evident. The OHT found in Drake does indeed exhibit characteristics similar to the observed transport (Fig. 1, bottom-left panel): an essentially zero high-latitude OHT in the Southern Hemisphere but a weak high-latitude transport in the Northern Hemisphere, together with a subtropical OHT peak that is larger in the Northern Hemisphere than in the Southern Hemisphere. Of note is the fact that the heat transport and its partition in DDrake are nearly indistinguishable from those of Drake: the introduction of a second barrier barely modifies the zonal-average climate (this is discussed further below). The solution in DDrake, however, is far richer than in Drake due to its more complex geometry. As seen in Fig. 2, OHTs and freshwater transports

(FWTs) in the small and large basins of DDrake have a striking similarity to those observed in the Atlantic and Indo-Pacific sectors of the modern climate. As we shall see, this is because dense water formation and deep convection become confined to the small basin in Drake. A direct consequence is that the overturning circulations in the ocean and OHT, although nearly identical to their Drake counterparts on the global scale, become concentrated in the small basin. It appears that geometrical constraints, albeit highly simple ones, are sufficient to endow DDrake with conspicuous features of the present climate in both the zonal average and at basin scale.

The Aqua solution is described in detail in Marshall et al. (2007). The sequence Aqua → Ridge → Drake is discussed in Enderton and Marshall (2009). Here, we compare Drake and DDrake and discuss what we can learn about the role of the ocean in climate from them. We describe the model configuration and formulation in section 2. The solutions are presented in more detail in section 3. In section 4 we explore the localization of deep ocean convection in the small basin of DDrake. In section 5, we conclude.

2. Description of the coupled model

We use the Massachusetts Institute of Technology (MIT) GCM in a coupled ocean–atmosphere–sea ice setup (Marshall et al. 1997a,b). The model exploits an isomorphism between the ocean and atmosphere dynamics to generate an atmospheric GCM and an oceanic GCM from the same dynamic core (Marshall et al. 2004). The model uses the following (isomorphic) vertical coordinates: the rescaled pressure coordinate p^* for the compressible atmosphere and the rescaled height coordinate z^* for the Boussinesq ocean (Adcroft and Campin 2004). As described in Adcroft et al. (2004), both component models use the same cubed-sphere grid at a low-resolution C24 (24×24 points per face, yielding a resolution of 3.75° at the equator). The cubed-sphere grid avoids problems associated with the converging meridian at the poles and ensures that the model dynamics at the poles are treated with as much fidelity as elsewhere. Additionally, it greatly simplifies the implementation of a conservative interface between the two GCMs (see Campin et al. 2008).

The atmospheric physics is of “intermediate” complexity, based on the simplified parameterizations primitive-equation dynamics (SPEEDY) scheme (Molteni 2003) at low vertical resolution (five levels). Briefly, this method comprises a four-band radiation scheme, a parameterization of moist convection, diagnostic clouds, and a boundary layer scheme. The 3-km-deep, flat-bottomed ocean

model has 15 vertical levels, increasing from 30 m at the surface to 400 m at depth. Effects of mesoscale eddies are parameterized as an advective process (Gent and McWilliams 1990) and an isopycnal diffusion (Redi 1982), both with a transfer coefficient of $1200 \text{ m}^2 \text{ s}^{-1}$. Convective adjustment, implemented as an enhanced vertical mixing of temperature and salinity, is used to represent ocean convection (see Klinger et al. 1996). The background vertical diffusion is uniform and set to $3 \times 10^{-5} \text{ m}^2 \text{ s}^{-1}$.

The sea ice model is based on the Winton (2000) two-and-a-half-layer thermodynamic model. The prognostic variables are ice fraction, snow and ice thickness, and a two-level enthalpy representation that accounts for brine pockets and sea ice salinity, employing an energy-conserving formulation. There is no sea ice dynamics. The land model is a simple two-layer model with prognostics temperature, liquid groundwater, and snow height. There is no continental ice. The land albedo is set 0.25 plus a contribution from snow, if present. The snow albedo parameterization (identical over land and sea ice) depends on the snow height, surface temperature, and snow age. Orbital forcing and CO_2 levels are at present-day values. The seasonal cycle is represented but there is no diurnal cycle.

The setup is very similar to that used in the studies of Marshall et al. (2007) and Enderton and Marshall (2009) with the following exceptions:

- 1) a coarser resolution (C24 instead of C32);
- 2) an implicit treatment of internal gravity waves in the atmosphere, permitting longer time steps; and
- 3) a shallower ocean (3 km instead of 5.2 km), which leads to a global ocean volume close to the present-day value and an equilibration time for the coupled system (controlled by ocean vertical mixing) that is $(5.2/3)^2 \simeq 3$ times shorter.

Points 1 and 2 allow one to increase the time step of the atmospheric model by a factor of $\simeq 3$ which, combined with point 3, leads to a coupled model that equilibrates about 9 times faster than the model used in Marshall et al. (2007). The coupled system can then be integrated for 1100 yr in 1 week of dedicated computer time. Fluxes of momentum, freshwater, heat, and salt are exchanged every hour (the ocean time step). Finally, note that, as discussed by Campin et al. (2008), the present coupled ocean–sea ice–atmosphere model achieves perfect (machine accuracy) conservation of freshwater, heat, and salt during extended climate simulation. This is made possible by the use of the z^* coordinate, which allows for a realistic treatment of the sea ice–ocean interface. This property is crucial to the fidelity and integrity of the coupled system.

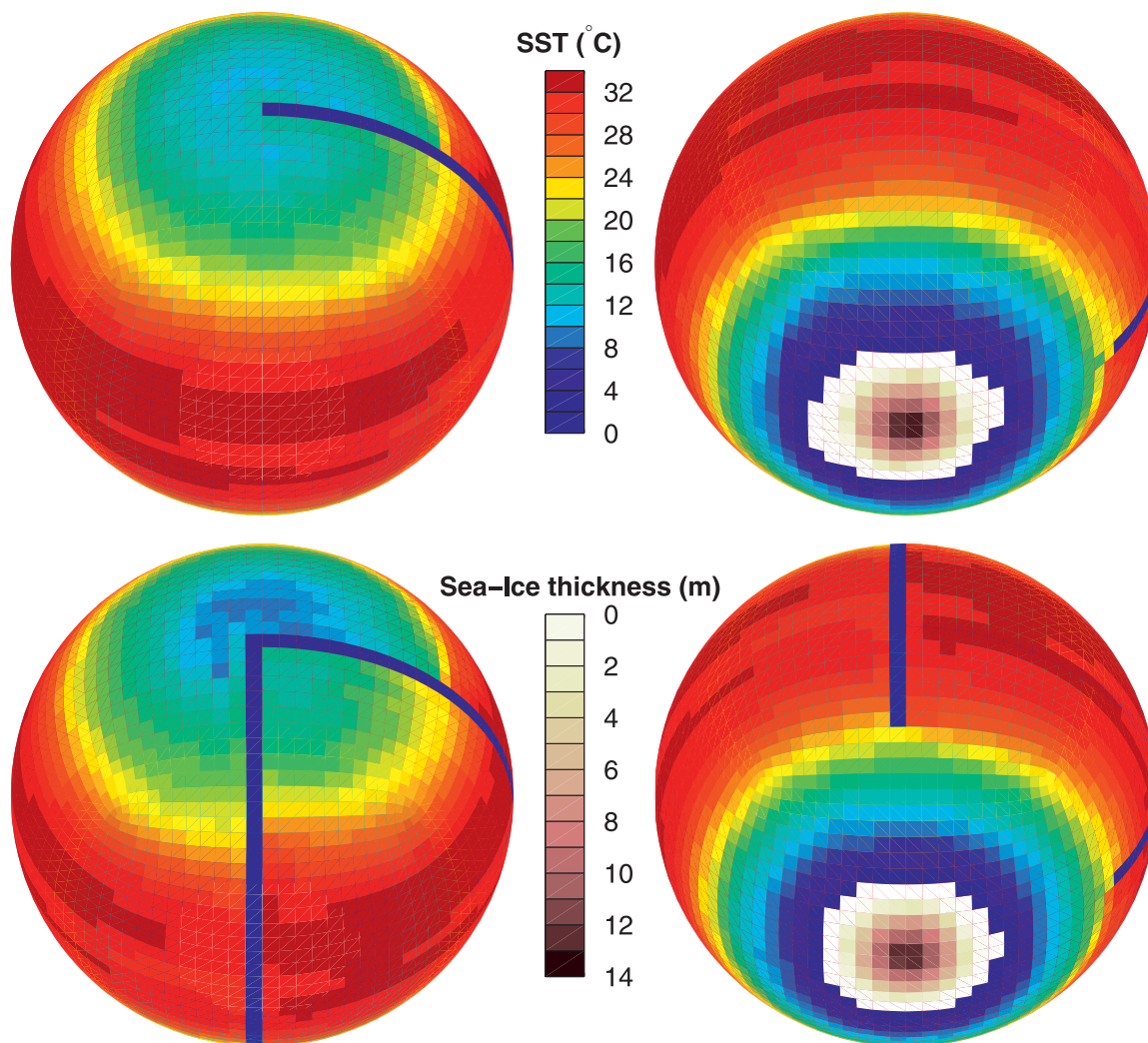


FIG. 3. (top) Drake and (bottom) DDrake solutions: the land barriers, annual mean SST, and perennial sea ice cover (minimum extent) are shown.

3. Climates of the Drake and DDrake configurations

a. Atmosphere and sea ice distributions

The configurations of the continents in Drake and DDrake are illustrated in Fig. 3. All diagnostics discussed here are averages over the last 50 yr of the coupled integrations, once they have reached equilibrium.

On the global scale, the climatologies of Drake and DDrake are remarkably similar. Both develop ice caps over the South Pole and exhibit similar meridional SST distributions (Fig. 3). The zonal mean atmospheric states of the two simulations are nearly indistinguishable as illustrated in Fig. 4, which shows the zonal wind and potential temperature fields. We observe westerly jet streams centered around 40° , reaching 40 m s^{-1} at 250 mb, flanked by trade winds and polar easterlies.

Temperature gradients are weak in the tropics, but strong baroclinic zones (in thermal wind balance) extend from about $\pm 15^\circ$ up to the poles. Note the colder southern pole favored by the absence of oceanic meridional barriers south of 35°S and further enhanced by the growth of sea ice over the South Pole. This leads to larger meridional gradients, especially near the surface and, thus, larger thermal wind shear. The surface winds, maintained against surface damping by a more intense baroclinic activity (see Fig. 16 below), are also stronger in the Southern Hemisphere. Combined with the larger thermal wind, this results in a Southern Hemisphere jet stream that is stronger than its northern counterpart, by up to 9 m s^{-1} at 250 mb.

Zonal-mean differences between Drake and DDrake are more evident in the Northern Hemisphere, but even here they are small (typically less than 2 m s^{-1} or 1 K).

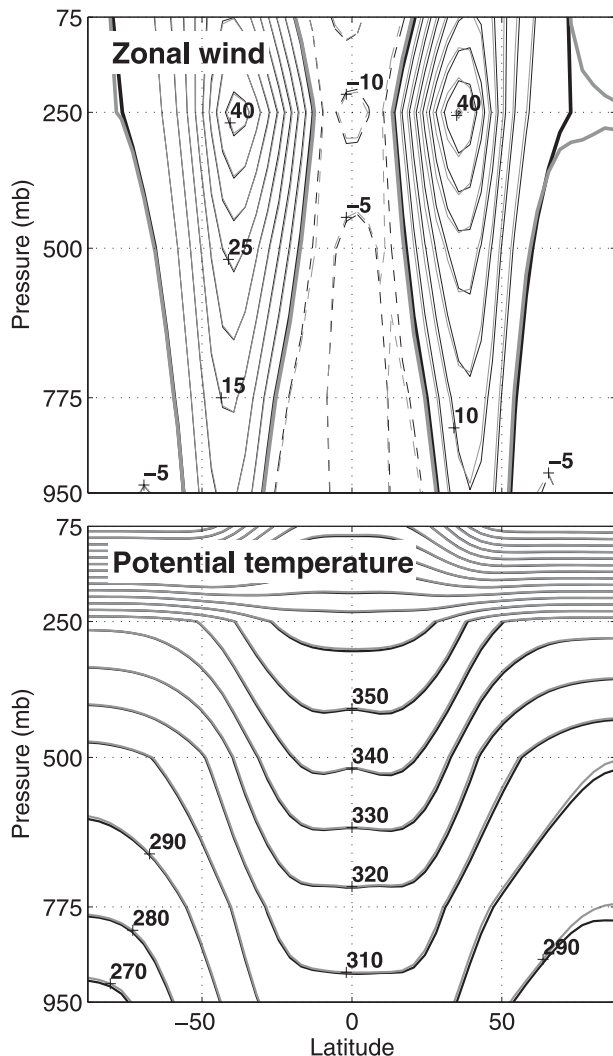


FIG. 4. Zonally averaged (top) annual-mean atmospheric wind and (bottom) potential temperature for Drake (black) and DDrake (gray).

Admittedly, the zonal mean smoothes out the differences. Indeed, the introduction of a second meridional barrier in the Northern Hemisphere of DDrake results in a slight shift of the jet stream near 90°E (not shown), but the resulting wind anomalies are rather small, peaking at 6 m s^{-1} at 250 mb. Above the boundary layer, zonal asymmetries in potential temperature have the same pattern as wind anomalies. However, near the surface they exhibit structures related to SST and ocean circulation changes, as discussed below.

In the Southern Hemisphere, Drake and DDrake develop nearly identical sea ice caps. Their perennial components extend to about 70°S with a maximum thickness of about 14 m at the South Pole (Fig. 3). In winter, seasonal cover, typically a meter thick, extends

to 60°S in August–September. No sea ice forms in the Northern Hemisphere.

b. Ocean

Although more differentiated than in the atmosphere, the circulations of Drake and DDrake in the ocean are again rather similar when viewed globally (Fig. 5). The upper 1000 m of the ocean is strongly stratified with the notable exception of the North Pole, where deep convection occurs (see below). Between 50°S and 50°N , the stable stratification of the upper ocean is due to temperature (note the salinity surface maxima near 30°C created by the large evaporation under the descending branches of the Hadley cells). South of 50°S , there is a temperature inversion due to the presence of sea ice. Here, the stable stratification (comparable in strength to that found in the midlatitudes) stems from salinity, which reaches a minimum of 26.4 psu at the surface over the South Pole. The deep ocean (below 1000 m), however, is weakly stratified with temperatures of about 9°C in Drake and 11°C in DDrake.

In the bottom panels of Fig. 5, we show the global residual-mean meridional overturning circulation (MOC), the sum of the Eulerian and (parameterized) eddy-induced streamfunctions. Again, Drake and DDrake are very similar. In both cases, the MOC exhibits two shallow subtropical wind-driven cells and a clockwise interhemispheric circulation extending from deep sinking regions over the North Pole southward to 50°S . Of the 30 Sv ($1\text{ Sv} \equiv 10^6\text{ m}^3\text{ s}^{-1}$) of dense water formed in the north, about one-third recirculates locally, one-third flows southward at depth and upwells at the equator, and the remaining third reaches the Southern Ocean, returning to the surface through Ekman suction under the westerly wind belt. Ultimately, some of this water returns to the northern high latitudes. Indeed, there is about 7–8 Sv of water looping around between the two hemispheres. Note that this interhemispheric circulation generates a northward heat transport that warms the Northern Hemisphere and cools the Southern Hemisphere, contributing to the formation of the sea ice caps over the South Pole. This is the “Drake Passage effect” described in Toggweiler and Bjornsson (2000, see also Toggweiler and Samuels 1995). Note that here the impact on temperature is larger, by about a factor 2, than that found in their calculations (not shown). This may be because a sea ice component and a dynamical atmosphere are employed here while Toggweiler and Bjornsson (2000) did not have a representation of sea ice and used an energy-balanced model.

The similarity of the two global overturning streamfunctions might lead one to expect the circulations of the two basins in DDrake to be rather similar. In fact, they

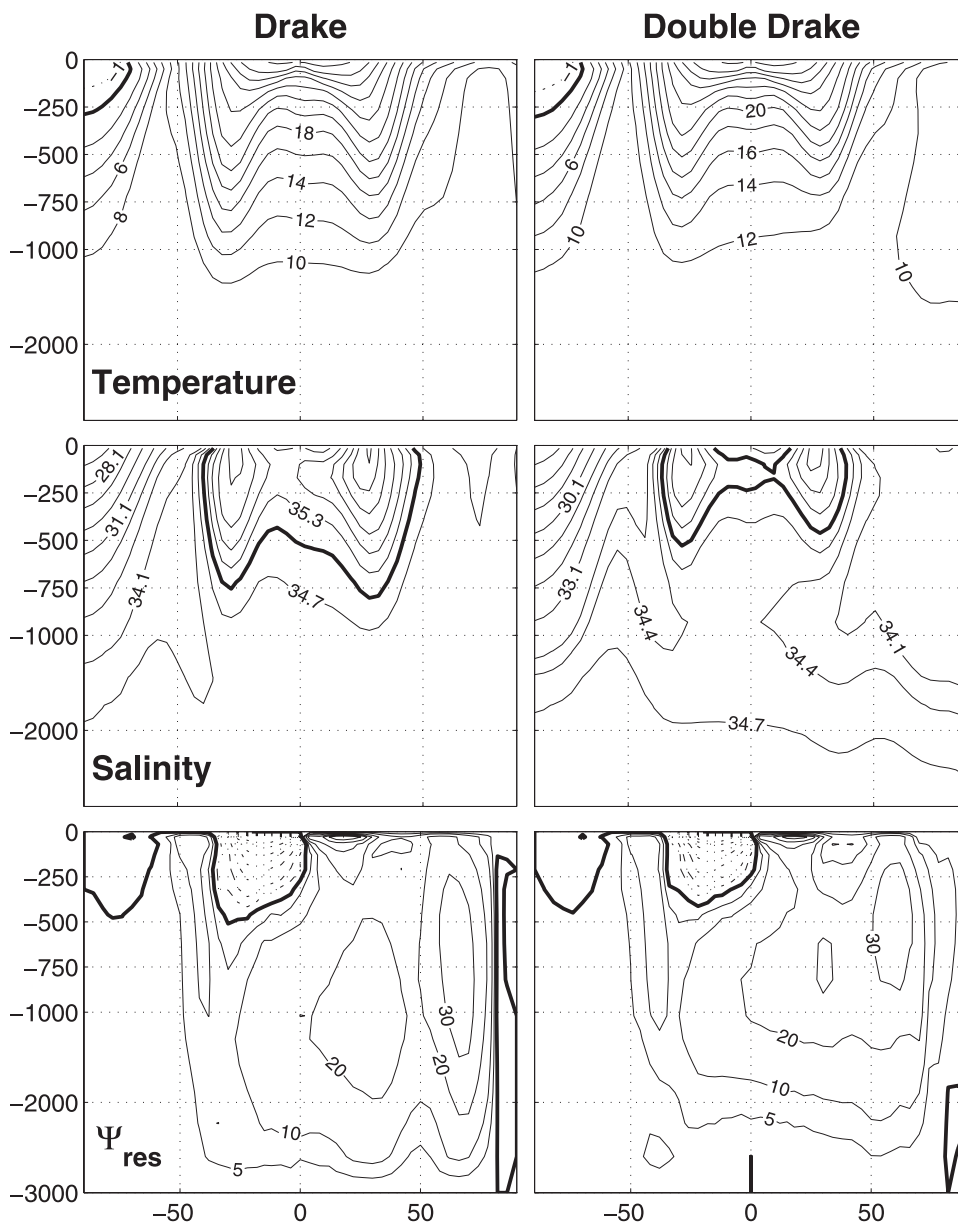


FIG. 5. Zonal-mean (top) temperature ($^{\circ}\text{C}$), (middle) salinity (psu), and (bottom) residual overturning streamfunction (Sv) for (left) Drake and (right) DDrake. Clockwise and counterclockwise circulations are denoted by solid and dashed-dotted lines, respectively. The zero contour in the temperature and streamfunction and the 35 contour in salinity are highlighted. Note the stretched vertical axis between 0 and 1000 m.

develop radically different circulations, as shown in Fig. 6. The small basin is dominated by a deep-reaching clockwise cell extending from the North Pole to the southern margin. This circulation is associated with the formation and export of dense water from the north. The two subtropical Ekman cells in the small basin are dominated by this convectively driven cell. In the large basin, however, wind-driven shallow cells are a primary feature and there is no circulation associated with deep

water formation. Note the northward intrusion of bottom water (~ 10 Sv) at the entrance of the basin, half of which returns to the Southern Ocean at middepth with the remaining part upwelling at the equator. This counterclockwise circulation partly cancels the deep branch of the clockwise circulation of the small basin. This explains why the interhemispheric global cell appears slightly shallower in DDrake than in Drake (Fig. 5).

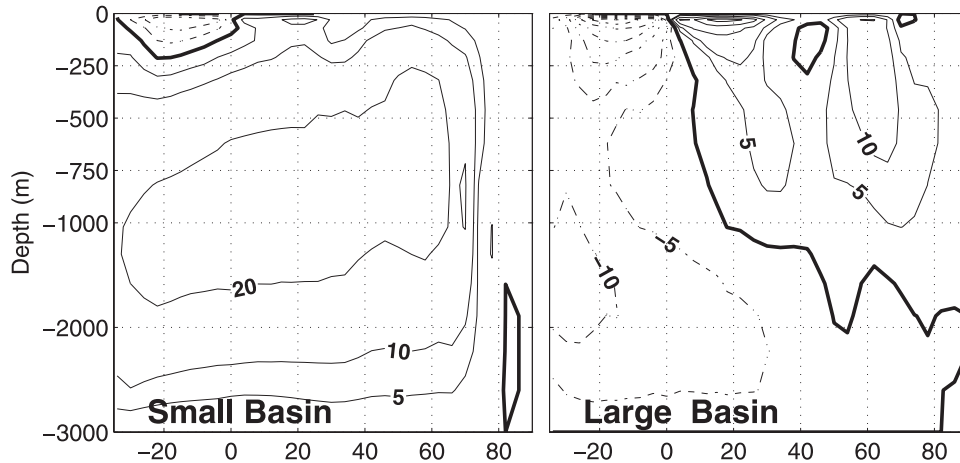


FIG. 6. Residual overturning streamfunctions in the (left) large and (right) small basins of DDrake.

c. Meridional transports

The heat and freshwater transports of the solutions reflect the main features of the respective circulations: the global transports of Drake and DDrake are nearly identical while the two basins of DDrake have radically different transports (see Figs. 2 and 7).

The atmospheric heat transport reaches its extrema in midlatitudes at the core of the jet stream/storm track (Fig. 7, bottom). Note the slightly stronger heat transport in the Southern Hemisphere (6 PW compared to 4.6 PW in Northern Hemisphere), which is associated with a more vigorous storm track (see Fig. 16 below). In the ocean, the maximum heat transports are associated with the subtropical Ekman cells (Fig. 7, top). The absence of meridional barriers south of 35°S leads to a near-zero heat transport at 50°S while the transport is about 1 PW at 50°N. Note also the small cross-equatorial northward heat transport (about 0.3 PW) due to the interhemispheric overturning cell.

By conservation, ocean and atmospheric freshwater transports must mirror one another (Fig. 8, top). To emphasize this, it is useful to express the atmospheric moisture transport as a volume transport: one atmospheric Sverdrup transporting the same mass as one oceanic Sverdrup, that is, 10^9 kg s^{-1} [$=1000 \text{ kg m}^{-3} \times 10^6 \text{ m}^3 \text{ s}^{-1}$, as done in Czaja and Marshall (2006)]. Figure 8 shows that the Drake and DDrake FWTs are identical. Their pattern simply reflects that of evaporation–precipitation (middle): evaporation peaks near 25°–30° of latitude under the descending branches of the Hadley cells where relatively dry upper-tropospheric air is brought into contact with the surface of the ocean. These locations also correspond to relative minima in precipitation and maxima in surface salinity. Precipitation peaks near the equator in the intertropical convergence zone and

poleward of 40° in association with the midlatitudes storm tracks. It is noteworthy that the global FWTs in our coupled system have some realism both in magnitude and pattern (Wijffels et al. 1992; Wijffels 2001). The slight asymmetry between the hemispheres (larger extrema in the Southern than the Northern Hemisphere) is also seen in the observations and is probably due to a stronger storm track in the Southern Hemisphere.

As seen in Fig. 2, the OHTs and FWTs in the individual basins of DDrake are very different from one

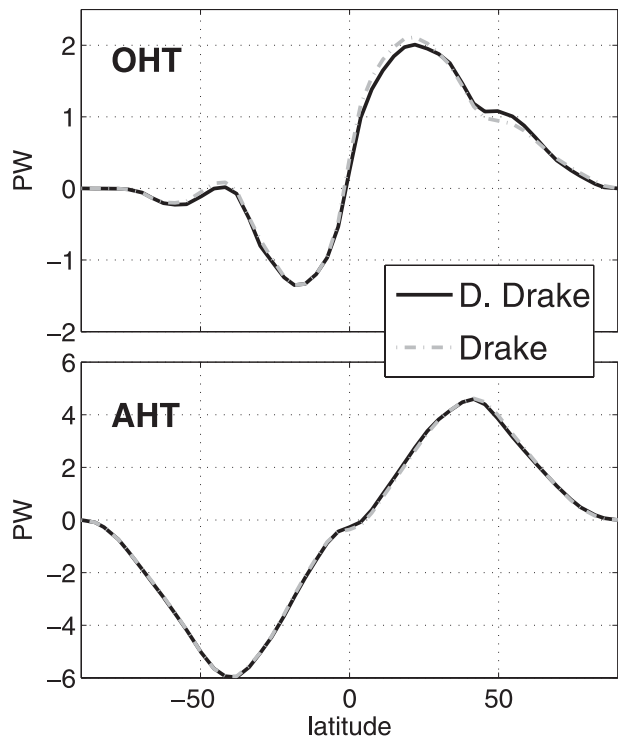


FIG. 7. (top) Oceanic and (bottom) atmospheric heat transports (PW) for the Drake and DDrake experiments.

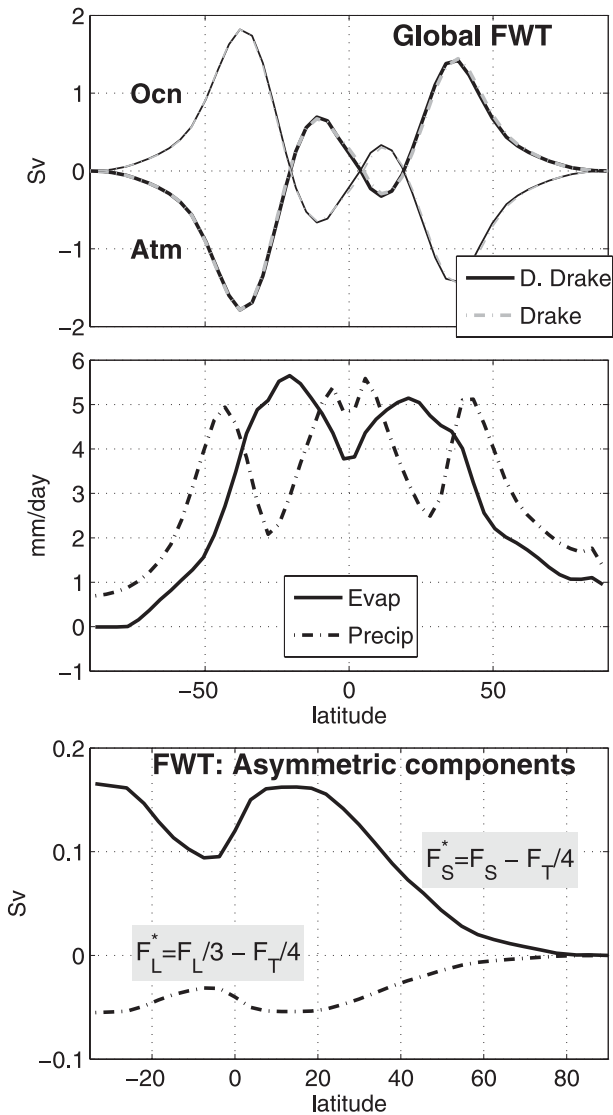


FIG. 8. (top) Atmospheric (thick) and oceanic (thin) freshwater transports in Drake and DDrake (Sv; see text). (middle) Zonal-mean precipitation and evaporation in DDrake (mm day^{-1}). (bottom) Asymmetric components of the freshwater transports in DDrake (see text for details).

another, even though their sum is very similar to the global transport found in Drake (Fig. 7). The small-basin OHT is everywhere northward while that of the large basin retains an asymmetric shape with respect to the equator (Fig. 2, left). These characteristics simply reflect the overturning circulations of the two basins seen in Fig. 6. In the small basin, the OHT is dominated by the deep clockwise circulation carrying warm subsurface water northward and returning cold dense water at depth. The Ekman subtropical cells make a smaller contribution, noticeable in the modulation of the north-

ward transport from 0.2 PW near 20°S to 1 PW at 20°N. In contrast, the large basin OHT is dominated by shallow wind-driven cells, although deep circulation contributes a slight asymmetry, enhancing the southward OHT in the Southern Hemisphere.

The large northward OHT in the small basin, especially when considering its small width, is responsible for one of the most notable atmospheric asymmetries introduced by the presence of a second ridge. Figure 9 displays the surface air temperature difference between DDrake and Drake. At the basin scale there is a striking pattern: above the small basin, DDrake is warmer by 0.5–1 K while over the large basin it is colder, especially near the North Pole. We also observe the smaller-scale imprint of oceanic features such as western boundary currents at $\pm 30^\circ$ near 90°E, and an equatorial cold tongue in the large basin near 50°E. Note that some of the strongest changes seen along 90°E are artificial, being associated with ocean to land changes on moving from Drake to DDrake. Nevertheless, the total temperature fields remain strongly zonally symmetric even in DDrake (not shown). However, Fig. 9 illustrates that the modified ocean circulation significantly alters the climate over the small basin, at least in the lower troposphere.

The FWT decomposition is less striking than that of OHT because transports in both basins retain a shape similar to the global one, reminiscent of the evaporation–precipitation pattern (Fig. 2, right). This is also true of the observed FWTs of the Atlantic and Indo-Pacific basins [Fig. 2, bottom right, after Wijffels et al. (1992); see Wijffels (2001) for other estimates]. Note that the Bering Strait transport has been removed as it is absent from our configuration. The small southward transport at the northern limit of the Atlantic sector reflects the net precipitation over the Arctic region. It should be noted that these observations have large uncertainties, possibly up to 0.3 Sv (see Wijffels 2001). That said, the observed and DDrake FWTs exhibit an interesting similarity: the transport of the small basin/Atlantic is more “northward” than that of the large basin/Indo-Pacific almost everywhere. Exploiting its idealized geometry, this effect is easily quantified in DDrake by computing the zonally asymmetric component of the transports. Defining the mean transport of a 90° wide-sector as the total transport divided by 4, $F_T/4$, the asymmetric part of the small- and large-basin transports, F_S^* and F_L^* , are then $F_S^* = F_S - F_T/4$ and $F_L^* = F_L/3 - F_T/4$, respectively (Fig. 8). By definition, $F_S^* + 3 \times F_L^*$ is zero. The small-basin zonal anomaly F_S^* is northward everywhere with a magnitude of about 0.15 Sv at the basin entrance, while that of the large basin is ~ 0.05 Sv and southward everywhere.

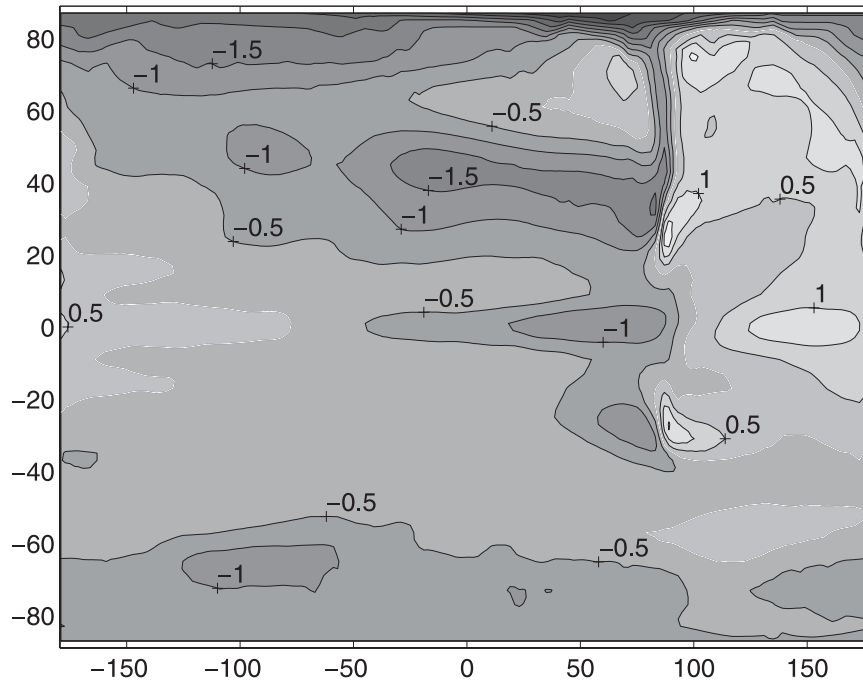


FIG. 9. Surface air temperature difference between DDrake and Drake (K). The zero contour is highlighted.

d. Localization of deep convection

As anticipated from the overturning circulations in Fig. 6, deep convection in DDrake is only observed in the small basin. Figure 10 shows the convective index averaged over the top 600 m for both Drake and DDrake. The index indicates the percentage of time over which convective adjustment is operative. In Drake, deep convection is distributed, more or less uniformly, over all longitudes. In contrast, deep convection in DDrake is absent from the large basin: a small amount of convection is observed, but it is relatively shallow. Below 250 m, convection is confined to the small basin where it reaches as deep as 1500 m about 15% of the time, typically one winter month per year.

This major difference in the convection sites between Drake and DDrake can readily be related to the properties of the surface water. As illustrated in Fig. 10 (bottom), the densest waters in Drake (about $\sigma \sim 26$) are found at the North Pole at all longitudes. (In fact, the temperature and salinity, except close to the land barrier, are almost zonally symmetric in Drake.) In DDrake, however, the densest water (also $\sigma \sim 26$) is found in the small basin only. Surface waters in the large basin are lighter by 0.5–1 kg m^{-3} . This contrast between the two basins is largely due to salinity. The small basin of DDrake is saltier than the large basin (Fig. 11). At the surface, the salt contrast between the two basins is

maximum at high latitudes, reaching 2 psu [about the same as the salinity contrast between the surface Atlantic and Pacific Oceans at high latitudes; see, e.g., Warren (1983)], and decreases southward to vanish near the equator. Note that the salinity contrast is partly compensated by the temperature as SSTs are warmer in the small basin. This was anticipated from the large northward heat transport of the small basin (Fig. 7) with a signature in the boundary layer air temperature (Fig. 9). The SST contrast is largest also near the pole (about 5°C) and vanishes close to the equator. Despite this, the salinity effect “wins out” and surface waters are denser in the small basin.

At depth, the contrast between the two basins is even more striking. In the nearly adiabatic ocean interior, water masses move away from their formation location conserving their temperature–salinity (T–S) properties. In particular, they are shielded from the fast-moving atmosphere, which tends to homogenize surface properties across the two basins (especially here where land is reduced to narrow strips). In DDrake, we observe the warm salty (dense) water formed near the North Pole moving southward below 1000 m in the small basin. Also, note the tongue of freshwater entering the small basin near 750 m, a feature that is barely noticeable in the large basin. This is a signature of the upper branch of the MOC drawing in low-salinity water subducted on the equatorward flank of the Atlantic Circumpolar Current. These low-salinity waters probably contribute, through

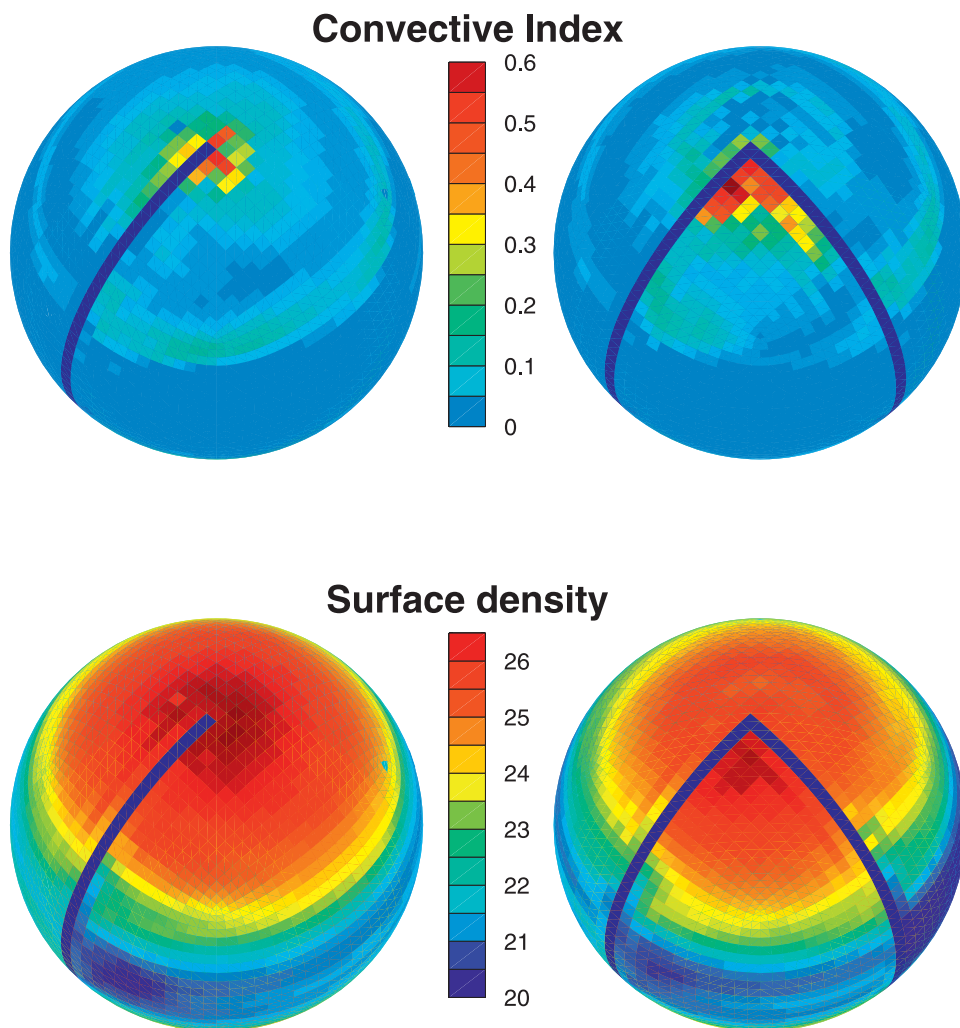


FIG. 10. Convective index vertically averaged over the (top) top 600 m and (bottom) surface density in (left) Drake and (right) DDrake.

mixing, to the lowering of deep water salinity values as waters move southward. In contrast, in the large basin, we observe high-salinity water (34.7, originating in the small basin) migrating northward near the bottom, and ultimately diffusing away as it mixes with fresh subsurface (1000 m) water originating from the polar region of the large basin.

It should be emphasized that the salinity contrast between the two basins is consistent with the freshwater transports seen in Fig. 8. The small basin has an anomalous freshwater import from the Southern Ocean and the large basin an anomalous export. By conservation, these are associated with proportionally higher freshwater fluxes into the atmosphere over the small basin than over the large basin, hence the salinity contrast.

To summarize, the introduction of a second barrier barely modifies the global climate of the coupled system,

as illustrated by the unchanged global transports of heat and freshwater. It leads, however, to a massive reorganization of the ocean circulation. Notably, all deep water formation and deep MOC become located in the small basin, which achieves a disproportionate amount of the northward heat and freshwater transport. This clearly results from the higher salinity in the small basin compared to the large basin.

4. Role of freshwater fluxes and salinity in DDrake

We now focus on the DDrake solution and attempt to identify the mechanism responsible for the salty small basin–fresh large basin, and hence the confinement of deep water formation to the small basin. As noted above, the small basin loses water to the atmosphere at a higher

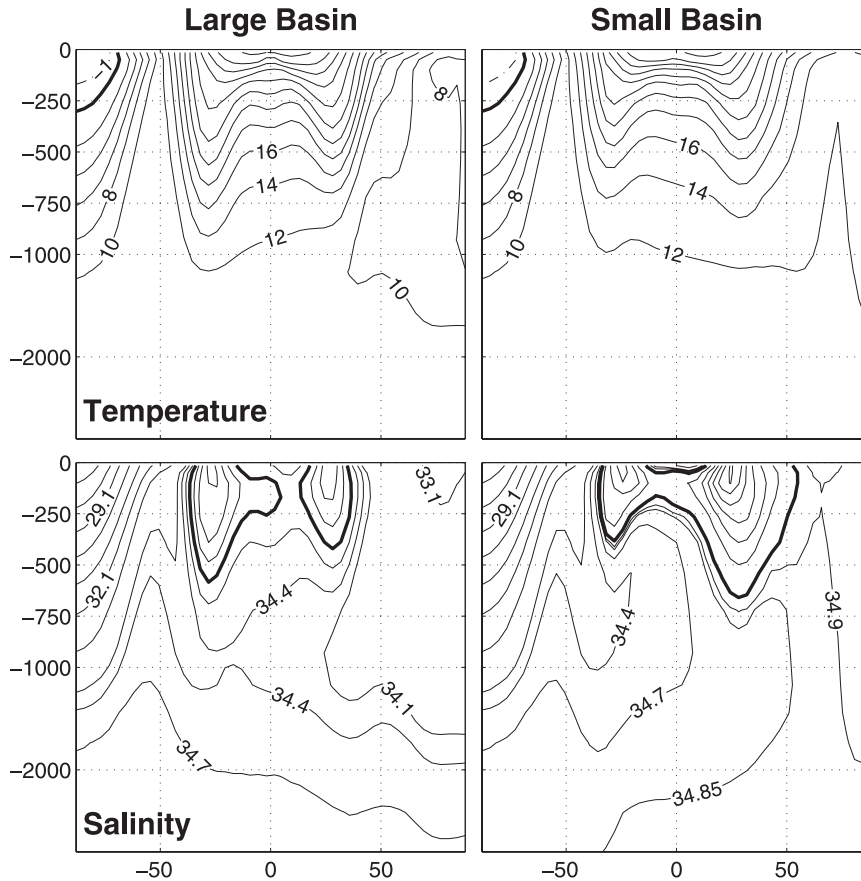


FIG. 11. Zonal-mean (top) potential temperature ($^{\circ}\text{C}$) and (bottom) salinity (psu) in the (left) large and (right) small basins of the DDrake. The zero contours for the temperature and 35 contour for salinity are highlighted.

rate than does the large basin. Thus, over time, the small basin becomes salty. Although both evaporation and precipitation exhibit asymmetries between the two basins, we show below that it is a deficit of precipitation over the small basin, and the different widths of the two basins, that explain the salt contrast.

a. Why is the small basin saltier?

Figure 12 shows the net (evaporation minus precipitation) freshwater flux as a function of latitude (top). The fluxes are integrated meridionally over 3° wide latitudinal bands and zonally across each basin. They have units of Sverdrups. In both basins, evaporation dominates in the subtropics, while precipitation dominates in the deep tropics and high latitudes. The patterns of the net surface freshwater flux in the two basins are indeed very similar. As anticipated from the widths of the basins, the net flux over the small basin (gray) is about 3 times smaller than that over the large basin (dashed). This emphasizes that, to first order, the magnitudes of the evaporation/precipitation patterns are not altered by

basin geometry. The scaling between the fluxes of the two basins is, however, not exactly one-third, as shown by the solid black line (Fig. 12, top). When positive, this curve indicates a relatively higher rate of freshwater flux out of the small basin and thus a tendency toward salinification. It shows that the small basin has a deficit of freshwater flux at all latitudes, except for a narrow equatorial band that sees enhanced freshening. The maximum tendency toward salinification is found in the Northern Hemisphere between 20° and 60°N , but the Southern Hemisphere has a significant contribution around 20°S .

These results are consistent with Fig. 8 as they are the air-sea flux equivalent to the anomalous freshwater transports F_S^* and F_L^* . However, as shown in Fig. 12 (bottom), the air-sea flux form can provide additional information if it is further decomposed into a contribution from evaporation (gray) and precipitation (dashed). The solid curve is the same as that shown in the top panel of Fig. 12. The precipitation term is multiplied by minus one, so that for both terms a positive value corresponds to a salinification tendency, either because of enhanced

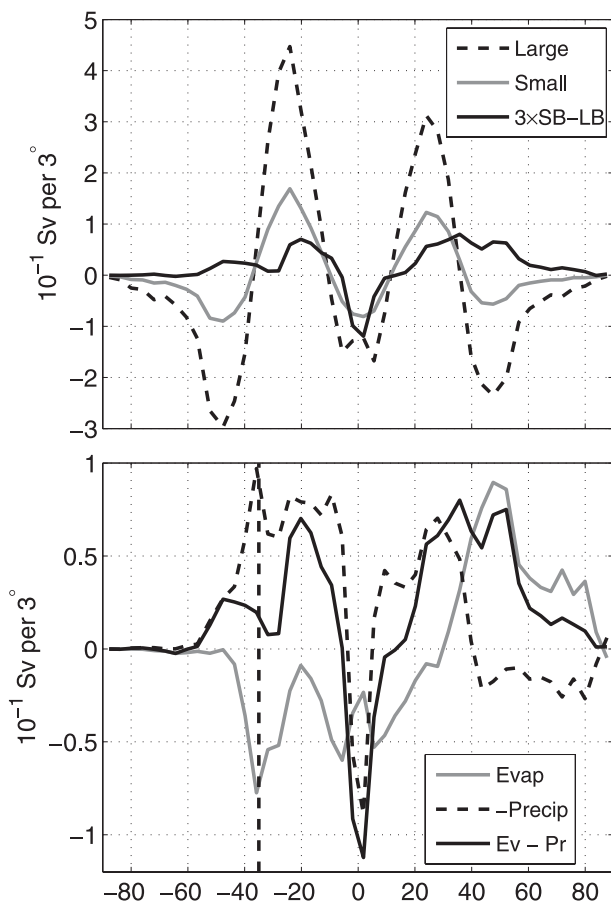


FIG. 12. (top) Net (evaporation minus precipitation) surface freshwater flux as a function of latitude in DDrake for the small basin (gray), the large basin (dashed), and the difference between 3 times the small basin flux and the large basin flux (solid). (bottom) The evaporation (gray) and precipitation (dashed) contributions to the difference (solid). The latter is identical to the solid line shown in the top panel. The air-sea fluxes are integrated zonally over the basin widths and meridionally over a 3° wide band and thus are in Sv per 3° band. Note that the vertical scale on the plots is in tenths of an Sv. The vertical dashed line near 35° S indicates the southern extent of the basins.

evaporation or a deficit of precipitation. The broad pattern of the evaporation anomaly is essentially a consequence of the SST difference between the two basins: warmer in the northern latitudes of the small basin but slightly warmer (by typically 0.5°C) in the tropics of the large basin (notably because of the warm pool found there). The salinification of the small basin northward of 30°N is due to enhanced evaporation over the small basin. However, this in itself is not enough to affect the salinity: the evaporated water needs to be carried by atmospheric winds and rained out into the large basin. If all the extra evaporation were precipitated locally, there would be a latent heat flux into the atmosphere but no net effect on the salinity. The asymmetric component of

the precipitation (dashed) shows that there is indeed anomalous precipitation over the small basin north of 40°N , but it is weaker than the evaporation, suggesting that some of the evaporated water is carried away, most likely by zonal winds.

The subtropics exhibit a rather different behavior. Typically around $\pm 20^\circ$, the evaporation anomaly is negative or small and salinification of the small basin is due to a deficit of precipitation. The deep tropics (5°S – 5°N) is a place where both anomalous evaporation and precipitation act to freshen the small basin. This is due to the presence of a large warm pool on the western side of the large basin (Fig. 16): strong evaporation from the warm pool results in a high atmospheric moisture content, which is readily advected by the trade winds across the land barrier into the small basin.

Figure 12 is suggestive of various mechanisms that contribute to net anomalous “extraction” of freshwater from the small basin. However, it is difficult to go further since Fig. 12 does not give any indication of how moisture is transported meridionally within each basin by the atmosphere. Enhanced evaporation over the small basin appears to be a key element, particularly because it occurs at high latitudes where salinity is critical to the localization of deep convection. But what causes the enhanced evaporation? Higher SSTs are the main factor here.² They are sustained by the strong northward OHT achieved in the small basin, itself resulting from a large MOC and deep convection in the small basin. However, this positive feedback mechanism could operate equally well in the large basin. If the large basin were to be warmer than the small basin and its overlying air more moist, zonal advection could extract water *regardless of the size of the basin*. If indeed the enhanced evaporation is the prime mechanism behind the localization of deep water formation, the implication is that a state with deep water formation in the large basin could be sustained (i.e., perhaps multiple equilibria are possible). In the following, we show that this is not the case. The relative rates of evaporation over the two basins play a minor role here. The key element is, in fact, the precipitation pattern.

b. Switching convection to the large basin

Here, we carry out an experiment to determine if a state with deep convection in the large basin is indeed stable. To achieve this, DDrake is initialized with the zonal mean temperature and salinity properties of the

² This is also the case in the Switch experiment below, but this may not be a general results. Other factors (e.g., wind magnitude, relative humidity) may also drive evaporation asymmetries between basins.

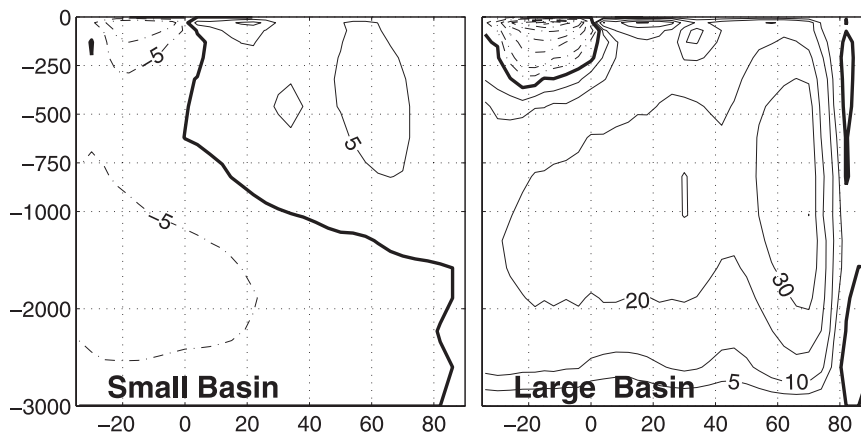


FIG. 13. Same as in Fig. 6, but for the initial time (year 20–50) of the Switch experiment. Units are in Sv.

two basins switched, $\bar{T}_{\text{small}}^x \leftrightarrow \bar{T}_{\text{large}}^x$, and likewise for salinity. A detailed description of the experiment is given in the appendix. The “Switch” experiment is run for 2000 yr. After an initial shock, the ocean indeed settles down into the expected state. Figure 13 shows the MOCs in the small and large basins averaged over years 20–50. A deep clockwise cell now dominates the large basin while the small basin exhibits shallow cells. The patterns are strikingly similar to those seen in Fig. 6, but reversed. Even secondary features such as the northward intrusion of bottom water seen in the large basin in Fig. 6 are now observed in the small basin. Note, however, that the magnitudes of the circulations in Figs. 13 and 6 are slightly different, probably because of the different widths of the basins.

As expected, because the large basin is now warmer, it has stronger evaporation and the surface air over it is moister than over the small basin (not shown). One might then expect the zonal wind to carry this air away, thus drawing water out of the large basin. If the enhanced evaporation is the prime mechanism controlling the freshwater flux asymmetry between the two basins, the high-salinity, deep water formation and deep MOC would be sustained in the large basin. However, the small basin still loses freshwater to the atmosphere at a higher rate than the large basin. Figure 14 shows the evolution of the net freshwater flux over the small and large basins as a function of time in the Switch experiment. A positive flux is a net loss to the atmosphere. Again, for comparison, the large basin flux is divided by a factor 3. From the very beginning, the small basin flux exceeds that of the large basin (0.55 compared to 0.42 Sv) although warmer SSTs and higher evaporation rates are found over the large basin.

This suggests that the state with deep water formation in the large basin is in fact unstable. Indeed, over

time the system slowly drifts back to the equilibrium state of the Control experiment. As deep convection and thus higher SSTs and enhanced evaporation return to the small basin, the freshwater asymmetry between the basins becomes more pronounced, increasing from 0.13 to 0.23 Sv. Thus, although the enhanced evaporation is not the primary reason for the localization of deep water formation in the small basin, it is a significant positive feedback. A crude estimate suggests that the evaporation contribution explains about 20%–25% of the freshwater asymmetry (see the appendix).

The equivalent of Fig. 12 (bottom), but for the initial stage (years 11–70) of the Switch experiment, is shown in Fig. 14 (bottom). As in the equilibrium of the Control experiment, the asymmetric component of the net freshwater flux at the surface is positive (i.e., in the sense to salinify) everywhere except near the equator. However, the split between evaporation and precipitation is now simpler: there is a deficit of precipitation everywhere over the small basin while evaporation tends to be higher over the large basin. In particular, we observe a dramatic change north of 40°N compared to Fig. 12. This indeed suggests that, at equilibrium in the Control experiment, the deficit of precipitation in the northern latitudes is “hidden” as some of the water due to enhanced evaporation is precipitated locally. The freshening of the small basin at the equator is a consequence of the warm pool reestablishing itself quickly (within years) after the switch.

c. Atmospheric moisture pathways

The Switch experiment demonstrates that the size of the basin is key to the localization of deep water formation. Furthermore, it shows that the “warm SST–evaporation” effect is secondary: it is a deficit of precipitation that

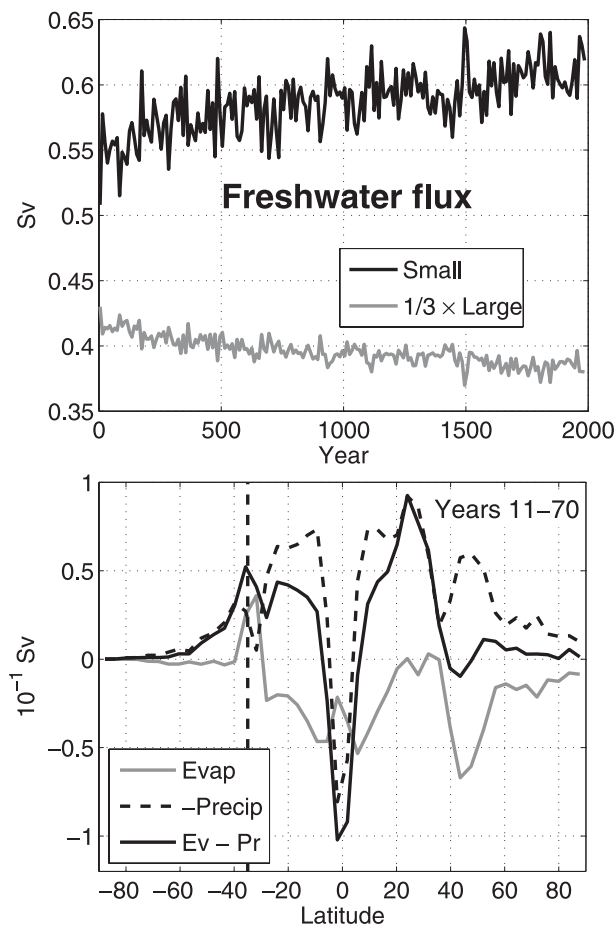


FIG. 14. (top) Net surface freshwater flux integrated over the small and large basins (Sv) as a function of time in the Switch experiment. A positive value corresponds to a net loss of water to the atmosphere. The large-basin value is scaled down by a factor 3. (bottom) Same as in the bottom panel of Fig. 12, but for the initial time of the Switch experiment.

leads to the salinification of small basin. But how is this achieved?

First, we observe that the freshwater deficit is not due to export from the small basin into the Southern Ocean. At equilibrium, the atmosphere carries 1.39 and 0.33 Sv southward over the entrance of the large and small basins, respectively, at 35°S. The average southward transport at this latitude is 0.43 Sv for a 90° wide sector. In fact, the atmosphere has a relatively low rate of moisture export at 35°S over the small basin. Therefore, the leak of precipitable water is achieved by zonal transport across the meridional land barriers.

Figure 15 shows the zonal transports of moisture over the land barriers at 90°E and 180° for the equilibrium Control simulation (left) and the initial time of the Switch simulation (right). The meridional axis is split into five areas according to the direction of the zonal winds (see

Fig. 15 caption). In the Control experiment, the outgoing zonal transport is larger than the incoming one over all latitudinal bands. The Switch experiment shows a convergence of moisture over the small basin at high latitudes, consistent with warmer polar SSTs and moister air over the large basin. This suggests that the high-latitude divergence seen in Control is due to enhanced evaporation there.

Using observations, Zaucker and Broecker (1992) estimated that the tropics (24°S–24°N) and the northern midlatitudes (north of 24°N) make a similar contribution, of about 0.17 Sv each, to the atmospheric freshwater export out of the Atlantic basin drainage. They drew attention, however, to the importance of the trade winds around 15°N, which achieve a relatively large fraction of the export aided by the low elevation of Central America. In our Control run, the exports of freshwater out of the small basin are 0.18 and 0.05 Sv in the tropics and the northern midlatitudes, respectively, showing a relatively larger contribution for the tropics in our simulation compared to observations. Notwithstanding, the large uncertainties in the observational estimates, one might speculate that the dominance of the tropics in our simulations reflects the fact that both the southern and northern trades are unblocked in DDrake, unlike in the real world.

The transports of moisture in Fig. 15 follow the mean circulation pattern. In the tropics, the mean flow is probably the main agent of transport. In the midlatitudes, however, synoptic-scale eddies and the shape of the storm track may play a role. A hint of this is seen in Fig. 16, which shows the standard deviation of the temperature fluctuations at 500 mb, bandpass-filtered between 2.5- and 10-day periods. The eddy activity has a broad maximum near 40°–45° in both hemispheres. While it is markedly zonally symmetric in the Southern Hemisphere, in the Northern Hemisphere it exhibits a minimum over the land barrier at 90°E, and a peak somewhat downstream of the western boundary of the large basin. We see then that the small basin storm track extends out of the basin, merging into the large basin storm track. In contrast, the storm track over the large basin dies out before reaching the small basin. This provides a “westward pathway” for the evaporated water to be carried and rained out into the large basin. In this regard, it is likely that the intense evaporation seen over the western boundary (see Fig. 16) plays a particular role by fueling this pathway. It should be noted, however, that because the bulk of the evaporation occurs near the transition between the easterlies and westerlies, around 20° (Fig. 16), water is carried northward/eastward and southward/westward into the large basin.

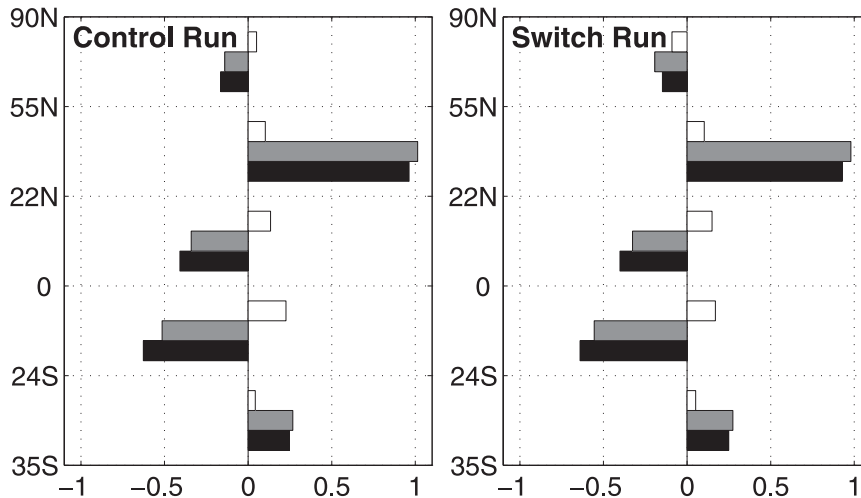


FIG. 15. Eastward (counted positive) or westward zonal transports of moisture over the land barriers for (left) the Control run and (right) the initial stage (years 11–70) of the Switch run. The meridional direction is split into five bands according to the zonal direction of the winds: southern westerly winds (35°–24°S), southern trade winds (24°S–0°), northern trade winds (0°–22°N), northern westerly winds (22°–55°N), and northern polar easterly winds (55°–90°N). The transports over the western (90°E) and eastern (180°) limits of the small basin are in black and gray, respectively, while their difference (east minus west) is shown in white. The latter is scaled up by a factor 2. A positive difference corresponds to a divergence of the transport and thus a net export of water out of the small basin.

In summary, the transport of moisture out of the basin is a consequence of the fact that not all evaporated water is precipitated locally: there is a precipitation fetch as moisture is transported away from the location of evaporation. For many air parcels, this fetch is long enough that water vapor acquired by evaporation over the small basin is rained out into the large one.

5. Conclusions

We have employed a parsimonious distribution of ocean barriers in an aquaplanet coupled model, to study the elemental character of the role of the ocean in climate. On moving from Aqua to Ridge to Drake to DDrake, a coupled climate is obtained that increasingly resembles our own. A major conclusion of our study is that, to a remarkable degree, the role of the ocean in climate is a consequence of two geometrical asymmetries: an interhemispheric asymmetry due to the presence of a “Drake Passage” and a zonal asymmetry due to the presence of a small basin and a large basin.

The zonal-mean climate is profoundly affected by the interhemispheric asymmetry. The opening of a gap in the Southern Ocean leads to a marked reduction in OHT to the South Pole: it thus becomes thermally isolated and a substantial ice cap grows. In contrast, in the Northern Hemisphere where a barrier reaches all the way to the pole, a weak OHT is found, albeit sufficient to

keep the North Pole ice free. With ice over the South Pole and none over the North Pole, there is a marked asymmetry in the pole-to-equator temperature difference in each hemisphere. This asymmetry is further enhanced by an interhemispheric MOC, driving a northward OHT at the equator. This MOC is associated with ocean deep convection in its sinking branch near the North Pole and wind-driven upwelling in the Southern Hemisphere over the latitudes of the gap. Although the geometrical constraints are applied to the ocean circulation only, their influence is clearly seen in the atmosphere: equator-to-pole air temperature gradients, storm tracks, and surface westerly winds are stronger in the Southern than in the Northern Hemisphere. These are all features of our present climate.

It is notable that the zonal-average climate and global transports of the ocean and atmosphere are so similar in Drake and DDrake. One might expect the total heat transport to be insensitive to the details of the circulation. As discussed in Stone (1978) and Enderton and Marshall (2009), the total heat transport of an Earth-like planet essentially depends on the incoming solar radiation and mean planetary albedo (both unchanged from Drake to DDrake). More remarkable, however, is that the zonal-average atmosphere is oblivious to the presence of a second barrier and the major rearrangement of ocean circulation associated with it. This suggests that, to first order, many properties, and in particular evaporation

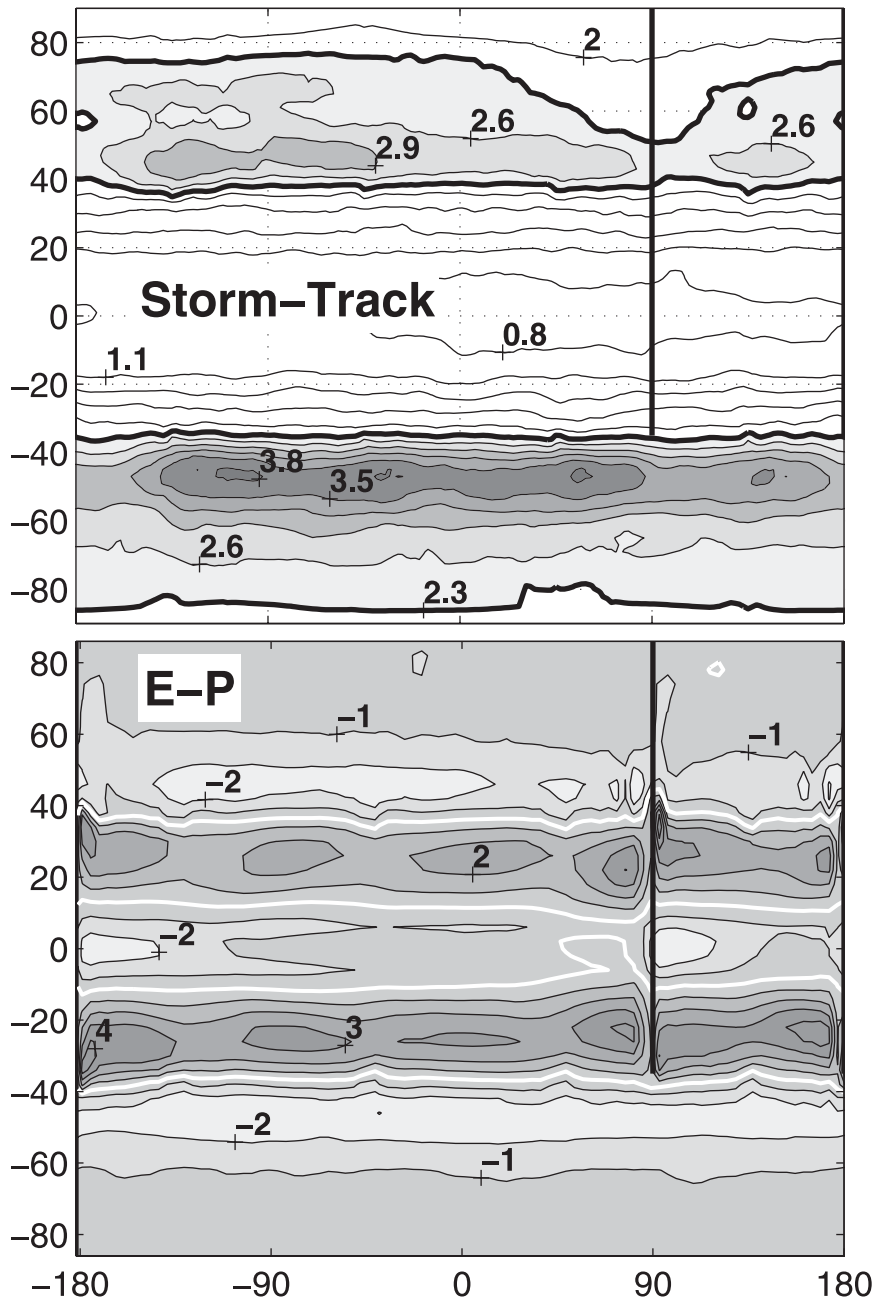


FIG. 16. (top) Standard deviation of the 500-mb temperature fluctuations filtered between 2.5 and 10 days (K). The contour interval is $0.3 K$ and values larger than 2.3 (marked by the thick black line) are shaded. (bottom) Time-averaged evaporation minus precipitation ($mm day^{-1}$). The contour interval is $1 mm day^{-1}$ and the zero contour is white.

and precipitation (and hence latent heat transport) on the global scale, are “controlled” by atmospheric dynamics with the ocean circulation responding. Additionally, it is also important to recognize that the bulk of the OHT is due to its wind-driven components, notably the Ekman-driven overturning cells in the subtropics (see Czaja and Marshall 2006). It therefore essentially varies

with the zonally integrated wind over the ocean, and, if the winds remain the same, the OHT can only be altered by reducing the fraction of a latitude circle occupied by the ocean.

The ocean circulation and regional climate, in contrast, are very sensitive to the zonal asymmetry (i.e., the presence of a small and a large basin). In Drake,

deep convection and deep water formation are confined to the small basin. This endows DDrake with conspicuous features of the present climate: a deep-reaching thermohaline circulation analogous to North Atlantic Deep Water and a vigorous, shallow, wind-driven circulation and no deep convection in the large basin, analogous to the Pacific Ocean. This translates into OHT features seen in the observations: northward transport at all latitudes in the small, Atlantic-like basin and a transport that is antisymmetric across the equator in the large, Pacific-like basin.

The localization of deep water formation to the small basin is a consequence of its high salinity, itself due to a deficit of precipitation over the basin. The fetch of the rain and the zonal transport of moisture in the atmosphere combine with the small width of the basin to create an anomalous transfer of freshwater from the small to the large basin. The trade winds are the major contributor to the freshwater export; although, both our simulations and observations (e.g., Zaucker and Broecker 1992) suggest that the Northern Hemisphere westerly winds make a significant contribution. Note that the export of freshwater from the small to the large basin is of order 0.1 Sv. This is about $1/10$ th of the magnitude of the meridional FWT (~ 1 Sv), which itself results from the cancellation of precipitation and evaporation fluxes, each typically reaching 10 Sv.

Our calculations should also be seen in the context of the debate about the relative roles of ocean and atmosphere in keeping Europe warm (Seager et al. 2002; Rhines et al. 2008). The introduction of a second barrier in Drake to form DDrake does change the local climate: the northern latitudes of the small basin offer a milder climate than those of the large basin. The analogy with the mild climate of western Europe is difficult not to draw. However, the simplicity of the geometry employed here, resulting for example in very weak atmospheric stationary waves, make it difficult to make a straightforward comparison. It is also worth putting our results in the light of discussions of the absence of deep water formation in the Pacific. Warren (1983) argues that the low salinity of northern Pacific surface waters prevents them from sinking to depth even in the presence of intense wintertime cooling. The freshness results, he argues, from the large net air-sea freshwater input and slow flushing of surface waters over the North Pacific region (relative to its Atlantic counterparts). He goes on to attribute the large freshwater input to low evaporation rates over cold surface waters, which result from the weak import of warm subtropical water into the northern Pacific. Such effects are at work in our DDrake configuration, but we have seen that the rate of evaporation is not the key element. Revisiting Warren's

study using recent datasets, Emile-Geay et al. (2003) attributed the freshness of the North Pacific to an excess of precipitation, a conclusion more in accord with our results. However, they suggest this excess is due to the atmospheric moisture transport associated with the Asian monsoon. The latter is obviously not present in our simulation.

Finally, note that the more complex geometry of the real world certainly plays a role in the coupled climate dynamics. For example, one expects the width of continents and mountain ranges to modify the relative contributions of the tropics and the northern midlatitudes to the freshwater export out of the small basin. Similarly, because the Pacific is a shrinking basin with convergent boundaries, it is circled by mountain ranges whose impact on the precipitation fetch results in the Atlantic basin draining most of Eurasia and North America. This equalizing effect is absent from our model. However, the results reported here suggest that such processes may be secondary.

Acknowledgments. This research was supported by MIT's Climate Modeling Initiative and NSF's Division of Ocean Sciences. We gratefully acknowledge computational resources and support from the NASA Advanced Supercomputing (NAS) Division.

APPENDIX

Description of the Switch Experiment

In the "Switch" experiment, the zonal-mean T-S properties of the small basin are used to initialize the large basin, and vice versa. Since the Southern Ocean is almost zonally symmetric, this manipulation barely modifies its state. Note, however, that because the higher salinity of the small basin now occupies the large basin, the global salt content is slightly increased in the Switch experiment: the global mean salinity rises from 34.56 in the Control run to 34.69 in the Switch run. This is believed to have a negligible impact on the solution because of the weak nonlinearities of the equation of state. The temperature manipulation for the initial conditions also entails a slight increase of the global heat content; however, the climate system being open for energy has the possibility to restore toward the temperature of the Control run.

Various indices of MOC and deep convection are shown in Fig. A1. For each basin, we monitor the strength of the MOC at high latitudes (the maximum MOC over 300–3000-m depth between 40° and 80°N) and of the cross-equatorial flow (the maximum MOC between 300 and 3000 m). As a proxy for the intensity of deep

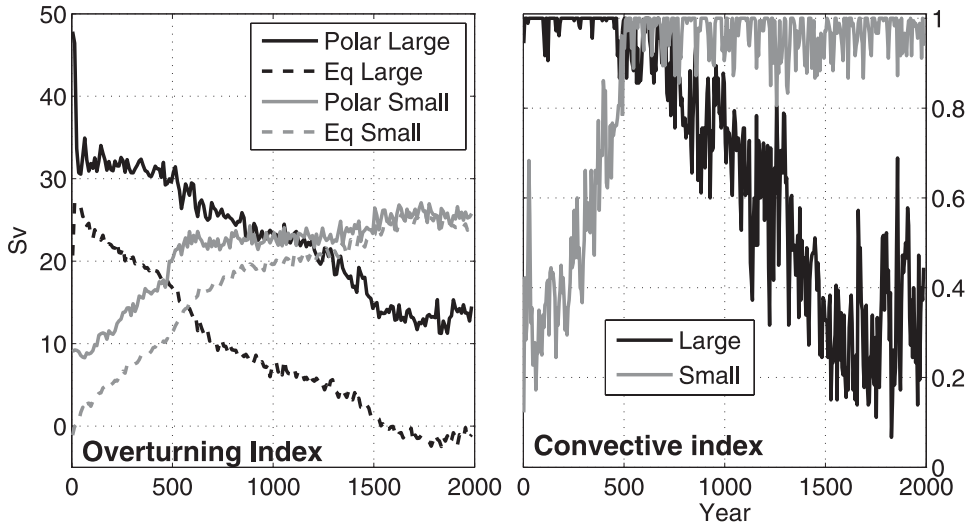


FIG. A1. Indices of (left) the overturning circulation strength (Sv) and (right) convection strength as a function of time in the Switch experiment. See text for details.

convection, we compute the average of the maximum convective index over 600–800-m depth (Fig. A1, right). Neglecting the initial shock, the strength of the MOC at high latitudes in the large basin settles around 32 Sv and remains relatively stable for about 500 yr. At the equator, however, the MOC decreases almost immediately. In the small basin, the MOC is initially weak, about 10 Sv at high latitudes, and null at the equator, but both indices increase, nearly linearly, from the beginning of the simulation. The convection indices illustrate that deep convection systematically occurs in the large basin, but only about 30% of the time in the small one. The former remains stable for about 500 yr while the latter rapidly increases in strength over that period.

A first transition occurs around 500 yr. The high-latitude MOC and deep convection in the large basin begin to decrease. In the small basin, the corresponding two indices stabilize. Note that the cross-equatorial MOC increases in the small basin and decreases in the large basin. A second transition occurs near 1500 yr as both high-latitude deep convection and cross-equatorial flow reach a plateau in the large basin.

Figure A2 illustrates the evolution of the temperature and salinity in the two basins. Averaged values for the whole basin and for the polar region only (north of 60°N) are shown. By construction, the large basin begins in a state that is warmer and saltier than the small basin one. From the very beginning, the system moves toward a reversal of the temperature and salinity characteristics of the basins. As the MOC of the small basin reaches its maximum near year 500, its temperature also stabilizes while the salinity increase changes from a linear trend to an exponential form. At 1500 yr, the stabilization of the

large basin MOC and deep convection triggers a third phase of adjustment, albeit a much weaker one than the previous two. The system appears to slowly drift back toward the equilibrium state of the Control run. This is clear for temperature, while for salinity, one needs to take into account the global salinity offset of 0.13 between the Control run and the Switch run. For example, the salt contrast between the two basins has decreased to about 0.37 at 2000 yr, compared to 0.32 in the Control run.

We can understand the transient behavior of the system by writing down a simplified equation for the salt content evolution of the small basin. We assume that water enters the basin at a rate ψ_i with the mean salinity of the Southern Ocean (S_{so}) and leaves it at a rate ψ_o with the mean salinity of the small basin (S_{sb}). Conservation of salt yields

$$\frac{\partial}{\partial t}[V_{sb}S_{sb}] = \psi_i S_{so} - \psi_o S_{sb}, \quad (\text{A1})$$

where V_{sb} is the volume of the small basin. Noting $\delta\psi$, the net freshwater flux through the surface of the small basin (positive into the atmosphere), conservation of volume gives

$$\frac{\partial}{\partial t}V_{sb} = \psi_i - \psi_o - \delta\psi. \quad (\text{A2})$$

The volume change of the basin is negligible as it only accounts for 1% of the salinity variations. Equation (A2) then simplifies to $\psi_i = \psi_o + \delta\psi$ and Eq. (A1) can be rewritten as

$$V_{sb} \frac{\partial}{\partial t}S_{sb} = (\psi_o + \delta\psi)S_{so} - \psi_o S_{sb}. \quad (\text{A3})$$

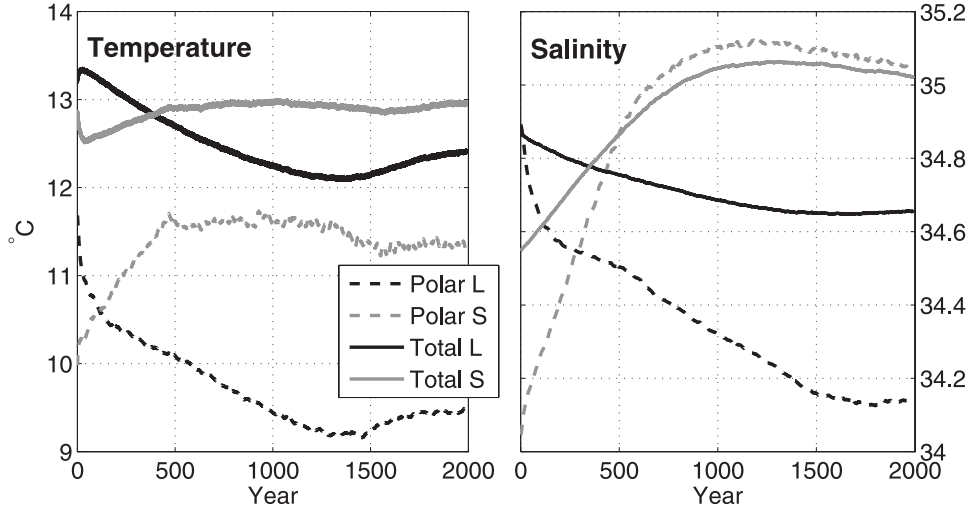


FIG. A2. (left) Temperature and (right) salinity indices for the Switch experiment as a function of time. The black and gray lines are for the small and large basins, respectively. Solid lines denote averages over the whole basin while dashed lines correspond to the polar regions only (north of 60°).

For a weak overturning, $\psi_o \simeq 0$, as in the first phase of the Switch experiment, Eq. (A3) gives

$$\frac{\partial S_{sb}}{\partial t} = \frac{\delta\psi}{V_{sb}} S_{so}, \quad (\text{A4})$$

and the model predicts a linear increase of the salinity. In this limit, the net loss of freshwater at the surface is compensated by an input of water from the Southern Ocean. The latter is associated with an import of salt, while there is no export. Hence, it predicts a linear increase of the salt content as is indeed observed up to year 500 of the Switch experiment. If a constant overturning is established in the basin, Eq. (A3) leads to

$$S_{sb} = S_1 e^{-\frac{\psi}{V_{sb}} t} + \frac{\psi + \delta\psi}{\psi} S_{so}, \quad (\text{A5})$$

where S_1 is an integration constant. A steady state is now possible as there is an export of salt by the overturning circulation, and the salinity then adjusts exponentially on a time scale V_{sb}/ψ . At equilibrium, there is a relationship between the salinities of the Southern Ocean and the small basin:

$$S_{sb} = \left(1 + \frac{\delta\psi}{\psi}\right) S_{so}, \quad (\text{A6})$$

which for a net evaporation, $\delta\psi > 0$, leads to $S_{sb} > S_{so}$. The equilibrium is achieved through a zero transport of salt into the basin: water enters the basin in a larger amount but at a smaller concentration than it leaves the basin.

This simple model gives a good qualitative description of the time evolution of the salinity in the small basin. Quantitatively, taking $\delta\psi = 0.56$ Sv, $S_{so} = 34.34$ and $V_{sb} = 2.83 \times 10^{17} \text{ m}^3$, predictions are $0.21 \text{ psu century}^{-1}$ for the linear rate of the initial phase $\partial S_{sb}/\partial t$ and 650 yr for the exponential time scale of the second phase V_{sb}/ψ (taking $\psi = 14$ Sv). The actual values are $0.07 \text{ psu century}^{-1}$ and 200 yr, obtained from a best fit over the periods 1–500 and 500–1500 yr, respectively. These values are typically a factor of 3 smaller than those predicted by the model. They can be both explained by the fact that the analytical model only considers the MOC as a possible agent of salt export while other neglected processes, such as gyre circulation or diffusion, certainly play a role in the numerical model. These additional exports slow down the linear buildup of salt in the first phase while allowing for a faster equilibration in the second phase. In fact, the equilibrium state of the Control run allows us to estimate an effective exchange rate (ψ_o^{eff}) between the small basin and Southern Ocean using Eq. (A6): $\psi_o^{\text{eff}} = S_{so}/(S_{sb} - S_{so})\delta\psi = 40$ Sv with $S_{so} = 34.34$, $\delta\psi = 0.6$ Sv, and $S_{sb} = 34.86$. This is indeed about 3 times larger than the MOC strength at 35°S in the small basin (about 14 Sv). In fact, the transport ψ_o is probably best thought of as the overturning strength computed in the salt coordinate. This is beyond the scope of the present paper.

Finally, from the freshwater fluxes time evolution (Fig. 14, top), we can make an estimate of the evaporation-feedback contribution to the basin asymmetry. Let us assume that the precipitation contribution P to the freshwater asymmetry is constant while the evaporation

contribution E plays one way initially and reverses at the end of the Switch run. Then, $P - E = 0.13$ Sv and $P + E = 0.23$ Sv, and hence $P = 0.18$ and $E = 0.05$ Sv. Thus, the evaporation contribution to the freshwater asymmetry is about 20%–25% at equilibrium.

REFERENCES

- Adcroft, A., and J.-M. Campin, 2004: Re-scaled height coordinates for accurate representation of free-surface flows in ocean circulation models. *Ocean Modell.*, **7**, 269–284, doi:10.1016/j.ocemod.2003.09.003.
- , J. M. Campin, C. Hill, and J. Marshall, 2004: Implementation of an atmosphere–ocean general circulation model on the expanded spherical cube. *Mon. Wea. Rev.*, **132**, 2845–2863.
- Barron, E. J., W. H. Peterson, D. Pollard, and S. Thompson, 1993: Past climate and the role of ocean heat transport: Model simulations for the Cretaceous. *Paleoceanography*, **8**, 785–798.
- Bryden, H., and S. Imawaki, 2001: Ocean heat transport. *Ocean Circulation and Climate*, G. Siedler et al., Eds., Academic Press, 455–474.
- Campin, J.-M., J. Marshall, and D. Ferreira, 2008: Sea ice–ocean coupling using a rescaled vertical coordinate z^* . *Ocean Modell.*, **24**, 1–14, doi:10.1016/j.ocemod.2008.05.005.
- Czaja, A., and J. C. Marshall, 2006: The partitioning of poleward heat transport between the atmosphere and ocean. *J. Atmos. Sci.*, **63**, 1498–1511.
- Emile-Geay, J., M. A. Cane, N. Naik, R. Seager, A. C. Clement, and A. van Geen, 2003: Warren revisited: Atmospheric freshwater fluxes and “Why is no deep water formed in the North Pacific”. *J. Geophys. Res.*, **108**, 3178, doi:10.1029/2001JC001058.
- Enderton, D., and J. Marshall, 2009: Explorations of atmosphere–ocean–ice climates on an aquaplanet and their meridional energy transports. *J. Atmos. Sci.*, **66**, 1593–1611.
- Gent, P. R., and J. C. McWilliams, 1990: Isopycnal mixing in ocean circulation models. *J. Phys. Oceanogr.*, **20**, 150–155.
- Klinger, B. A., J. Marshall, and U. Send, 1996: Representation of convective plumes by vertical adjustment. *J. Geophys. Res.*, **101** (C8), 18 175–18 182.
- Marshall, J., A. Adcroft, C. Hill, L. Perelman, and C. Heisey, 1997a: A finite-volume, incompressible Navier–Stokes model for studies of the ocean on parallel computers. *J. Geophys. Res.*, **102** (C3), 5753–5766.
- , C. Hill, L. Perelman, and A. Adcroft, 1997b: Hydrostatic, quasi-hydrostatic, and nonhydrostatic ocean modeling. *J. Geophys. Res.*, **102** (C3), 5733–5752.
- , A. Adcroft, J. M. Campin, C. Hill, and A. White, 2004: Atmosphere–ocean modeling exploiting fluid isomorphisms. *Mon. Wea. Rev.*, **132**, 2882–2894.
- , D. Ferreira, J. M. Campin, and D. Enderton, 2007: Mean climate and variability of the atmosphere and ocean on an aquaplanet. *J. Atmos. Sci.*, **64**, 4270–4286.
- Molteni, F., 2003: Atmospheric simulations using a GCM with simplified physical parametrizations. I: Model climatology and variability in multi-decadal experiments. *Climate Dyn.*, **64**, 175–191, doi:10.1007/s00382-002-0268-2.
- Redi, M. H., 1982: Oceanic isopycnal mixing by coordinate rotation. *J. Phys. Oceanogr.*, **12**, 1154–1158.
- Rhines, P., S. Häkkinen, and S. A. Josey, 2008: Is the oceanic heat transport significant in the climate system? *Arctic–Subarctic Ocean Fluxes*, R. R. Dickson et al., Eds., Springer, 87–109.
- Seager, R., D. S. Battisti, J. Yin, N. Gordon, N. Naik, A. C. Clement, and M. A. Cane, 2002: Is the Gulf Stream responsible for Europe’s mild winters? *Quart. J. Roy. Meteor. Soc.*, **128**, 2563–2586.
- Stone, P. H., 1978: Constraints on the dynamical transports of energy on a spherical planet. *Dyn. Atmos. Oceans*, **2**, 123–139.
- Toggweiler, J. R., and B. Samuels, 1995: Effect of Drake Passage on the global thermohaline circulation. *Deep-Sea Res. I*, **42**, 477–500.
- , and H. Björnsson, 2000: Drake Passage and paleoclimate. *J. Quat. Sci.*, **15**, 319–328.
- Trenberth, K. E., and J. M. Caron, 2001: Estimates of meridional atmosphere and ocean heat transports. *J. Climate*, **14**, 3433–3443.
- Warren, B. A., 1983: Why is no deep water formed in the North Pacific? *J. Mar. Res.*, **41**, 327–347.
- Wijffels, S. E., 2001: Ocean freshwater transport. *Ocean Circulation and Climate*, G. Siedler et al., Eds., Academic Press, 475–488.
- , R. W. Schmitt, H. L. Bryden, and A. Stigebrandt, 1992: Transport of freshwater by the oceans. *J. Phys. Oceanogr.*, **22**, 155–162.
- Winton, M., 2000: A reformulated three-layer sea ice model. *J. Atmos. Oceanic Technol.*, **17**, 525–531.
- Wunsch, C., 2005: The total meridional heat flux and its oceanic and atmospheric partition. *J. Climate*, **18**, 4374–4380.
- Zaucker, F., and W. S. Broecker, 1992: The influence of atmospheric moisture transport on the fresh water balance of the Atlantic drainage basin: General circulation model simulations and observations. *J. Geophys. Res.*, **97** (D3), 2765–2773.